Nanoscale

PAPER

View Article Online
View Journal | View Issue

Cite this: *Nanoscale*, 2024, **16**, 12982

Theoretical insights into single-atom catalysts for improved charging and discharging kinetics of Na–S and Na–Se batteries†

Mukesh Jakhar, *[a,b] Veronica Barone *[a,b] and Yi Ding[c]

Dissolution of poly-sulfide/selenides (p-S/Ses) intermediates into electrolytes, commonly known as the shuttle effect, has posed a significant challenge in the development of more efficient and reliable Na–S/Se batteries. Single-atom catalysts (SACs) play a crucial role in mitigating the shuttling of Na–pS/Ses and in promoting Na_2S/Se redox processes at the cathode. In this work, single transition metal atoms Co, Fe, Ir, Ni, Pd, Pt, and Rh supported in nitrogen-deficient graphitic carbon nitride (rg-C_3N_4) are investigated to explore the charging and discharging kinetics of Na–S and Na–Se batteries using Density Functional Theory calculations. We find that SAs adsorbed on reduced g-C_3N_4 monolayers are substantially more effective in trapping higher-order Na_2X_n than pristine g-C_3N_4 surfaces. Moreover, our *ab initio* molecular dynamics calculations indicate that the structure of X_8 (X = S, Se) remains almost intact when adsorbed on Fe, Co, Ir, Ni, Pt, and Rh SACs, suggesting that there is no significant S or Se poisoning in these cases. Additionally, SACs reduce the free energies of the rate-determining step during discharge and present a lower decomposition barrier of Na_2X during charging of Na–X electrode. The underlying mechanisms behind this fast kinetics are thoroughly examined using charge transfer, bonding strength, and d-band center analysis. Our work demonstrates an effective strategy for designing single-atom catalysts and offers solutions to the performance constraints caused by the shuttle effect in sodium–sulfur and sodium–selenium batteries.

Received 15th March 2024,
Accepted 13th June 2024

DOI: 10.1039/d4nr01134a

rsc.li/nanoscale

1. Introduction

The increased interest in electric vehicles and the widespread use of portable devices have prompted extensive research to develop more efficient energy storage technologies. While lithium-ion batteries currently dominate the battery market,[1] their continued expansion faces challenges related to raw materials supply, safety concerns linked to organic electrolytes, and high cost, among other factors.[2,3] At the same time, sodium (Na)-ion batteries are drawing more attention due to the low cost and abundance of Na compared to Li.[4–6] Sodium chalcogen batteries, specifically Na–S batteries, have been extensively studied and show promising potential for applications in next-generation sustainable energy storage systems.[7–9] While sulfur (S) and selenium (Se) are promising cathode materials due to their abundance and impressive volumetric capacities of 3467 mA h cm^{-3} and 3268 mA h cm^{-3}, respectively.[10–12] These battery technologies still face various challenges for practical applications. Some of these challenges are sluggish reaction kinetics, complex reaction mechanisms, and significant volume expansion during charge/discharge cycles.[13,14] To address these concerns, especially in preventing the shuttle effect, extensive research has focused on the idea of physical confinement and chemical adsorption that can effectively immobilize soluble intermediates.[15,16] Various low-dimensional materials have been incorporated to serve as the framework for the chalcogen (S, Se) cathode system such as carbon nanotubes,[17] graphene,[8,18] porous carbon,[9,19] polymers,[20] and other low-dimensional materials.[10] However, enhancing the affinity between the anchoring materials and both low (Na_2X_n; $n \leq 2$) and high order (Na_2X_n; $n > 2$) Na–polysulfide/selenides (Na–pS/Ses) is not sufficient to notably diminish the shuttle effect arising from the sluggish kinetics of immobilized Na_2S/Se. Hence, there has been a recent focus on accelerating conversion kinetics by optimizing the compounds involved in these reactions through the shift from insoluble Na_2S/Se to soluble extended-chain Na–pXs (X = S, Se).[21–23]

[a]*Department of Physics, Central Michigan University, Mt. Pleasant, MI 48859, USA. E-mail: baron1v@cmich.edu*
[b]*Science of Advanced Materials Program, Central Michigan University, Mt. Pleasant, MI 48859, USA*
[c]*U.S. Army DEVCOM-GVSC, Warren, MI 48397, USA*

† Electronic supplementary information (ESI) available: Phonon spectrum curves for SA@rg-C_3N_4; charge transfer and AIMD plot for the X_8 (X = S, Se) molecules; the optimized geometric configurations of Na–pXs (X = S, Se); geometric configurations of electrolyte solvent (DOL and DME); Gibbs free energy profile for sulfur/selenium reduction reactions (S/SeRRs); partial density of states (PDOS) of Na_2X–SA. See DOI: https://doi.org/10.1039/d4nr01134a

Single atom catalysts (SACs) have been studied as efficient catalysts for electrochemical reactions within metal–S/Se batteries as they exhibit homogeneous active sites, a high catalytic activity, and an optimal catalyst utilization compared to conventional nanocatalysts.[24] In order to prevent the aggregation of single atoms (SAs), a substrate that offers effective anchoring sites to trap these SAs is needed. Presently, SACs consisting of transition metal atoms supported on N-doped defective graphene is the most studied model for electrocatalysis in Li–S batteries to suppress the shuttle effect and improve the electrode electrochemical performance.[25–28]

Besides N-doped graphene, metal-free graphitic carbon nitride sheets (g-C_3N_4) have attracted attention owing to their unique porous structure and abundant sites for confinement of metal atoms facilitated by their high nitrogen concentration.[29–32] In fact, there have been several reports about utilizing SAs supported by g-C_3N_4 as reliable electrocatalysts for different reactions such as HER,[33] OER,[34] and Co_2RR.[35] Moreover, few results are also reported with N-coordinated Fe[36] and Ni[37] adsorbed on two-dimensional g-C_3N_4 for applications in Li–S batteries. However, due to the lack of the special anchoring sites, pristine g-C_3N_4 encounters some challenges in preventing the single metal atoms from aggregation. It has been reported that a stronger metal–support interaction can be achieved by introducing N-vacancies in the g-C_3N_4 monolayer to boost photocatalytic H_2 production,[38] nitrogen fixation,[39] and in bifunctional oxygen electrocatalyst applications.[34] To the best of our knowledge, there is no literature studying SACs in N-deficient graphitic carbon nitride for Na–S and Na–Se batteries.

This study systematically investigates the effect of SACs in the charging and discharging kinetics of Na–S and Na–Se cathodes through Density Functional Theory (DFT) calculations. To this end, we choose seven SA (Co, Fe, Ir, Ni, Pd, Pt, and Rh) adsorbed on a N-deficient graphitic carbon nitride (rg-C_3N_4) monolayer as SACs model systems. We also perform *ab initio* molecular dynamics (AIMD) simulations for X_8 (X = S, Se) species adsorbed on SACs models and discuss the interaction mechanism between the SAC and Na–pXs. Our calculations indicate that SACs can accelerate the discharging kinetics of sulfur and selenium reduction reaction and we also compare their effectiveness in the Na–S and Na–Se systems. Furthermore, an exploration of decomposition energy barriers and integrated crystal orbital Hamilton populations (ICOHPs) is conducted to compare the charging performance of the SACs models. In both, Na–S and Na–Se systems, SACs demonstrate a significantly improve charging and discharging performance. These findings can guide experimental investigations for exploration and implementation of SACs in energy storage systems.

2. Computational methods

Spin-polarized DFT calculations are performed using the Vienna *Ab initio* Simulation Package (VASP).[40,41] The exchange–correlation interactions are described using the gradient-corrected Perdew–Burke–Ernzerhof (GGA-PBE) functional[42] and the projector augmented-wave (PAW) method.[43] In addition, van der Waals interactions are included utilizing the Grimme DFT-D3 correction scheme.[44] For the plane-wave expansion, the cutoff energy is set to 520 eV. The SAC models are built by adsorbing single atom (SA) on a 2 × 2 × 1 supercell of a reduced graphitic carbon nitride monolayer (rg-C_3N_4). Monkhorst–Pack meshes with 3 × 3 × 1 *k*-points are used for geometric relaxation following previous theoretical studies of SA supported on g-C_3N_4.[45–47] During the geometric optimization of Na–pXs within the SACs models, relaxation of atomic positions is carried out with a constant cell shape until the residual force reaches a threshold of less than 0.01 eV Å^{-1}. A 20 Å vacuum space along the *z*-direction is considered to prevent interactions with adjacent periodic images. Our *ab initio* molecular dynamics (AIMD) simulations are conducted using the Nose–Hoover thermostat at room temperature (300 K) for X_8 (X = S, Se) species on the SACs models. The climbing image-nudged elastic-band (CI-NEB) method is used to calculate the decomposition energies of Na_2X.[48,49] Bader charge analysis is carried out to analyze the charge transfer between Na_2X and the SA.[50] Phonon dispersion curves are obtained using DFPT (density functional perturbation theory) and the PHONONPY packages.[51,52] The chemical bond analyses based on the Crystal Orbital Hamilton Population (COHP) method were conducted using the LOBSTER package.[53] The d-band center and Gibbs free energy correction is calculated using vaspkit.[54] The VESTA code was used for the visualization of geometric configurations and charge density differences.[55]

The adsorption energies (E_{ads}) of Na–pXs on the rg-C_3N_4 substrate was evaluated using the following equation[56,57]

$$E_{ads} = E_{Na-pXs} + E_{Substrate} - E_{Total}$$

where E_{Total}, $E_{Substrate}$, and E_{Na-pXs} are the energies of the Na–pXs (X = S, Se) adsorbed on the rg-C_3N_4 substrate, the isolated rg-C_3N_4 substrate, and an isolated Na–pXs molecule, respectively. According to this definition, a positive E_{ads} indicates a stable binding between molecule and substrate. Details on the Gibbs free energy calculations procedure are presented in ESI.†

3. Results and discussion

As shown in Fig. 1(a), SACs are modeled by embedding a SA on a N-deficient graphitic carbon nitride (SA@rg-C_3N_4) monolayer. The metals selected as SACs are Co, Fe, Ir, Ni, Pd, Pt, and Rh as they have been identified as the are most robust SACs based on their high thermodynamic, electrochemical, and thermal stability.[58] As depicted in Fig. 1(b), the lattice parameters (*a* and *b* for a 1 × 1 unit cell) of the SA@rg-C_3N_4 systems exhibit a significant increase compared to the pristine (*a* = 6.93 Å, *b* = 6.95 Å) and reduced (*a* = 6.91 Å, *b* = 5.94 Å) g-C_3N_4 monolayers. This volume expansion can be attributed

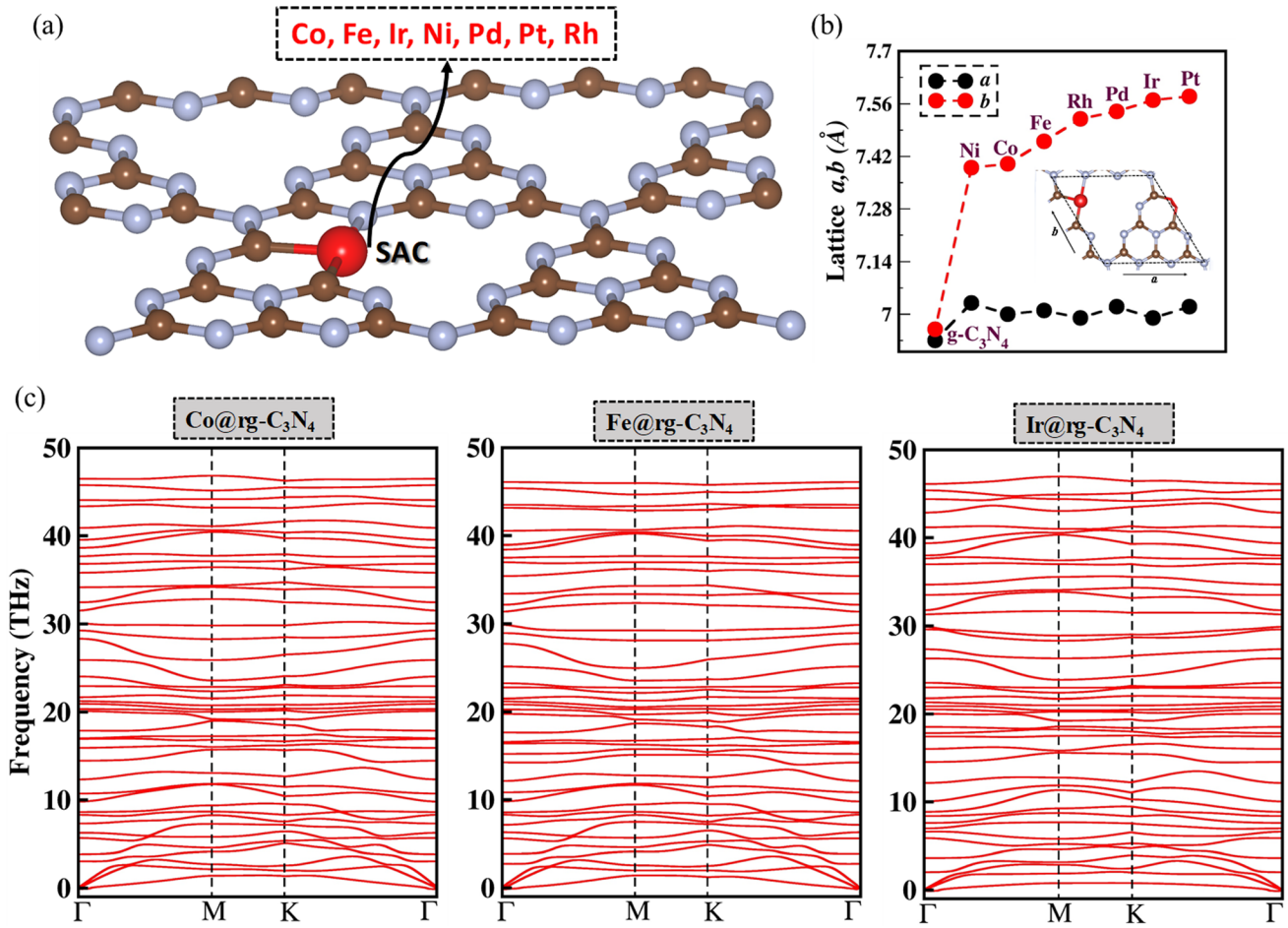

Fig. 1 (a) Perspective view of a SA adsorbed on the rg-C_3N_4 support. (b) Lattice constant of the SA@rg-C_3N_4 monolayer for a 1 × 1 unit cell as represented in the inset. (c) Phonon spectra curves of SA@rg-C_3N_4 for SA = Co, Fe, Ir.

to the large van der Waals radii of the SAs incorporated in the manolayer.[59] Additionally the optimized configuration and electronic band structure of g-C_3N_4 and rg-C_3N_4 monolayers are presented in Fig. S1.† In order to verify the dynamic stability of the SA@rg-C_3N_4 systems, we conducted an analysis of the phonon dispersion spectra. As illustrated in Fig. 1(c) for Co, Fe, and Ir, and Fig. S2† for the remaining SAs, no noticeable imaginary phonon modes are detected in the spectra, indicating the overall dynamic stability of all seven SA@rg-C_3N_4 systems.

3.1. Adsorption of X_8

Initially, the adsorption of X_8 (with X = S and Se) species is examined on pristine and reduced g-C_3N_4 as well as SA@rg-C_3N_4. The calculated adsorption energies are shown in Fig. 2(a), where we observe that the adsorption on all substrates is slightly stronger for Se_8 than for S_8, even though the overall trends are similar for the two cases. In both cases, the highest adsorption energy is obtained for the Fe catalyst and can be correlated to the shortest bond lengths Fe–S (2.16 Å) and Fe–Se (2.29 Å) among all SAC substrates. With the exception of Pd and Ni, the adsorption energies on the SAC surfaces of both S_8 and Se_8 structures are notably higher than on pristine and reduced g-C_3N_4 indicating that the incorporation of SACs can boost the capacity of g-C_3N_4 to load S and Se active materials. To further elucidate the adsorption mechanism of X_8 on the SAC substrates, the charge transfer between the X_8 molecules and the substrates is obtained (Fig. S4†). In the case of Pd and Pt catalysts there is a small charge transfer of approximately 0.016 electrons from S_8 to the substrate. For Fe, Co, Ir, Ni, and Rh SACs, the charge transfer is also small but occurs in the opposite direction, with approximately in the range from 0.047 to 0.13 electrons transferred from the substrate to S_8.

In order better understand the adsorption behaviour of S_8 and Se_8 at the early stages of discharge, AIMD simulations starting at the optimized adsorption configurations on various substrates are performed. After 5 ps, all adsorption configurations of S_8 and Se_8 on the SAC substrates (except on the Pd SAC) remain intact without any apparent migration or deformation (S_8 on the Fe SAC is shown as an example in Fig. 2(b)). However, our calculations indicate that for X_8 adsorption on substrates without metal atom catalysts (pristine and reduced g-C_3N_4 substrates), there is a substantial surface reconstruction

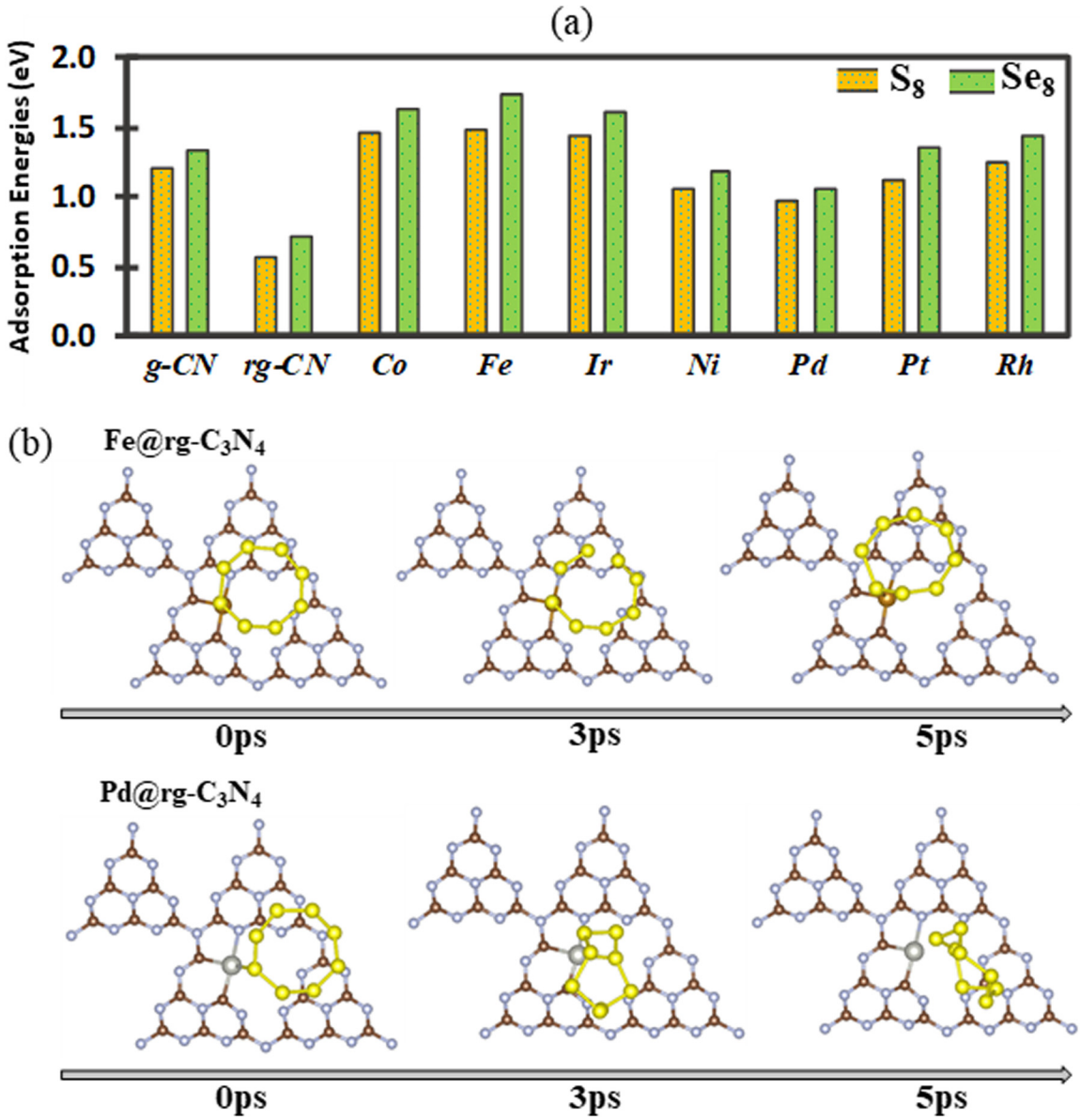

Fig. 2 (a) The adsorption energies of X_8 (X = S and Se) adsorbed on the surface of pristine, reduced g-C_3N_4, and SA@rg-C_3N_4 (SA = Co, Fe, Ir, Ni, Pd, Pt, and Rh). (b) Snapshot at 5 ps of AIMD simulations of the adsorption of S_8 on SA@rg-C_3N_4 for SA = Fe and Pd.

and deformation of the X_8 molecule. The AIMD snapshots of S_8 and Se_8 on various substrates are presented in Fig. S5 and S6,† respectively. The apparent migration and rotation of S_8 from the hollow cavity shown in Fig. 2(b) can be correlated to the lower adsorption energy of S_8 on Pd-based SAC compared to other SA catalysts. Our AIMD calculations indicate that up to 5 ps, the structure of X_8 remains almost intact when adsorbed on Fe, Co, Ir, Ni, Pt, and Rh SACs, suggesting that there is no significant occurrence of sulfur or selenium poisoning in these substrates.[28,60]

3.2. Adsorption of Na–pXs (X = S, Se)

During the discharge process, the interaction of Na cations with the X cathode can generate a series of intermediate compounds from Na_2X_8 to Na_2X (Na_2X_8, Na_2X_6, Na_2X_4, Na_2X_2, and Na_2X). Therefore, we also investigated the interaction between both insoluble species (Na_2X_n; n = 1, 2) and soluble species (Na_2X_n; n = 4, 6, 8) and the substrates to elucidate the role of the SAC in mitigating the poly-sulfide and selenide shuttle effect in Na–S and Na–Se electrodes. The optimized geometric configurations of all the Na_2X_n; n = 1, 2, 4, 6, 8 species are provided in Fig. S7† and the obtained X–X and Na–X bond distance agrees well with previous studies (Table S2†).[61–63] Fig. 3(a) shows the adsorption energies of Na_2X_n (n = 1, 4, 8) species on the surface of pristine (g-C_3N_4), reduced (rg-C_3N_4) and seven SA@rg-C_3N_4 catalysts. The most stable configurations of Na–pSs and Na–pSes adsorbed on various substrates are presented in Fig. S8 and S9,† respectively. The adsorption

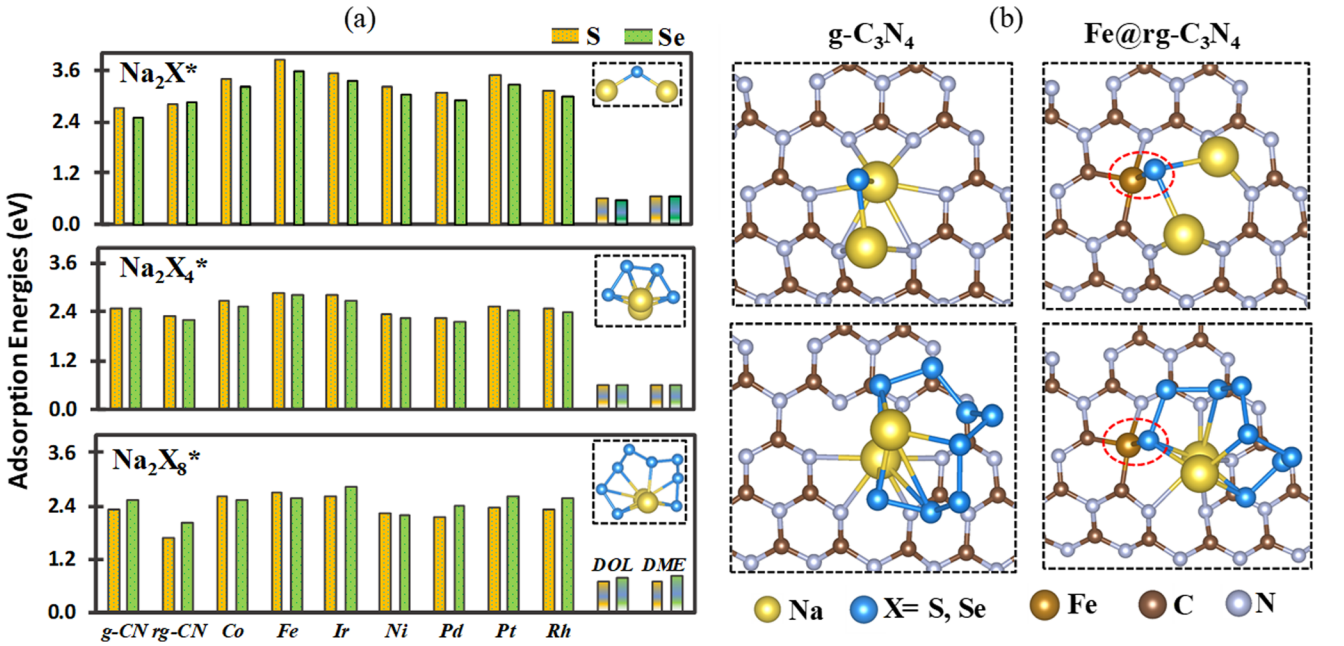

Fig. 3 (a) The adsorption energies of Na_2X_n (n = 1, 4, 8) adsorbed on SA@rg-C_3N_4. (b) Geometrical structures of Na_2X_n (n = 1, 8) adsorbed on a pristine g-C_3N_4 and Fe@rg-C_3N_4 monolayer.

configurations of Na–pXs for SACs are very similar. Both X and Na atoms contribute to their adsorption *via* SA–X and Na–N interactions, while the adsorption on pristine and reduced g-C_3N_4 primarily results only from the interaction between Na and N, which is further confirmed by the charge density analysis in section 3.4. Taking Fe SAC as a representative example, Fig. 3(b) shows that the Fe–S bond length is shortened from 2.18 Å (Na_2S_8) to 2.16 Å (Na_2S), suggesting an enhanced interaction in low-order Na–pXs. Moreover, the adsorption energies of insoluble Na_2X on the surface of SACs are in the range of 3.0–3.8 eV, significantly larger than on pristine and reduced g-C_3N_4 (2.5–2.8 eV), which indicates that the introduction of SAs can enhance the interaction of Na–pXs and rg-C_3N_4. For comparison, it is worth noting that Na–pSs (Na_2S_n; n = 1, 2, 4, 6) exhibit stronger adsorption energies than Na–pSes. However, Na_2Se_8 exhibits a larger adsorption energies than Na_2S_8. Among the SACs studied in this work, Fe@rg-C_3N_4 presents the strongest interaction for both Na–pSs and Na–pSes, with adsorptions energies surpassing numerous previously reported 2D sulfur hosts like graphene,[64] MXenes,[65] VS_2,[66] and As_2S_3.[67] Additionally, we have also computed the adsorption energy for Na_2X_3 species on pristine, reduced g-C_3N_4, and Fe SAC as shown in Fig. S10.† The observed trend of adsorption strength, with Na_2X_3 exhibiting greater affinity than Na_2X_4 and lesser affinity than Na_2X, closely mirrors findings reported in the literature for Li_2S_3.[68] It is interesting to compare the Na–pXs binding strengths on these substrates with the interaction energies of these species in commonly used electrolyte solvents such as 1,3-dioxolane (DOL) and 1,2 dimethoxymethane (DME).[69] The optimized configurations of DOL and DME with Na–pXs (X = S, Se) are shown in Fig. S11.† The interaction energies (0.58–0.81 eV)[65] between Na–pXs and DOL/DME are significantly lower than the adsorption energies (1.65–3.83 eV) of Na–pXs on SACs, suggesting that these SACs can effectively preclude Na–pXs shuttling in Na–S and Na–Se batteries.

In order to further understand the underlying physical mechanisms governing the interaction between Na–pXs and SAC, we examined the charge transfer of the adsorbed Na–pXs using Bader charge analysis. Our results (see Table S3†) indicate that overall, as sodiation progresses from Na_2X_8 to Na_2X, there is a gradual increase in the amount of charge transferred between the Na–pXs and the substrate. This result indicates that the interaction between each SAC substrate and Na–pXs becomes more robust with increased sodiation, which in turn could explain their greater adsorption affinity for lower Na–pXs. However, when comparing different substrates, we note that the charge transfer between Na–pXs and substrates is, in general, larger in pristine and reduced g-C_3N_4 than in the SACs substrates. As the binding energies of Na–pXs are significantly larger in the SACs substrates, it is then expected that the SACs substrates increase the covalency of the interactions compared to pristine and reduced g-C_3N_4.

3.3. Discharging performance of Na–S and Na–Se electrodes

To analyze the discharging performance of the electrodes, we next explore the sulfur and selenium reduction reactions on various g-C_3N_4 substrates. During the initial discharge process of a Na–S electrode, the solid-phase S_8 undergoes a transformation into a series of soluble Na–pSs (Na_2S_n; $4 \leq n \leq 8$), which are subsequently further reduced into insoluble Na–pSs (Na_2S_n; $1 \leq n \leq 3$).[70] As discussed previously, the electrochemical reaction mechanisms of Na–Se batteries is similar to

that of Na–S batteries, with the formation of Na–pSes as intermediate products and Na_2Se as the final discharge product.[10] The Gibbs free energy of each intermediate reaction step from S_8* to Na_2S* and from Se_8* to Na_2Se* over g-C_3N_4, rg-C_3N_4 and SA@rg-C_3N_4 (with SA = Co, Ir, and Fe) are shown in Fig. 4(a) and (b), respectively. The remaining Gibbs free energy plots for the reduction of Na–pSs and Na–pSes on SA@g-C_3N_4 (with SA = Rh, Ni, Pd, and Pt) are presented in ESI (Fig. S12†). Following current literature notation, * represents an active site on the catalytic substrate.

For both battery systems, the initial step corresponding to the reduction of X_8 to Na_2X_8 is an exothermic reaction regardless of the substrate, indicating the spontaneous nature of this conversion. All the following four reactions steps are endothermic reactions. Our calculations indicate that for g-C_3N_4, the limiting step corresponds to the transition from Na_2X_4 to Na_2X_2, and from Na_2X_2 to Na_2X in the rg-C_3N_4 substrate. A similar trend of limiting steps is observed in graphene and N-doped graphene for Li–S battery systems.[71] For Ir, Co, Fe, and Rh SACs, the last transition from Na_2X_2 to Na_2X is associated with a notably high positive Gibbs free energy barrier compared to other steps indicating the last reaction step as the rate determining (RD) step in the whole process. On the other hand, for SACs containing Ni, Pd, and Pt, the transition from a soluble Na_2X_4 to an insoluble Na_2X_2 is found to be the RD step as they present the highest energy barrier. In comparison to Na–S, Na–Se shows a superior reaction kinetics due to the lower RD step barrier for selenium reduction reactions on SACs. The RD step on the surface of SACs is significantly reduced, falling within the range of 0.68 to 1.0 eV, compared to the 1.17 eV and 1.01 eV for pristine g-C_3N_4 and rg-C_3N_4, respectively. The obtained RD step barriers for Ni, and Co, Ir, Fe, Rh are lower than for the reported highly active MXenes for Na–S batteries (0.85–1.23 eV)[72] and Na–Se batteries (0.80–1.4 eV).[61] Overall, the presence of a SA in conjunction with a rg-C_3N_4 support significantly enhances the discharging performance for the sulfur and selenium reduction reactions.

3.4. Charging performance of Na–S and Na–Se electrodes

The reaction kinetics during the charging process of Na–S and Na–Se electrodes are primarily governed by the decomposition of Na_2S and Na_2Se, respectively.[11] Therefore, reducing the decomposition barriers of Na_2X can significantly enhance the oxidation reaction kinetics and prolong the life cycle of the electrodes. We investigated the decomposition mechanisms of Na_2X oxidation ($Na_2X^* \rightarrow NaX^* + Na^+ + e^-$) using the CI-NEB method.[48,49] The energy profiles along the optimal reaction pathways for Na_2X decomposition are illustrated in Fig. 5(a) and (b). The barriers for the Na_2X decomposition on the SACs substrates (1.44–1.56 eV for Na_2S and 1.42–1.48 eV for Na_2Se)

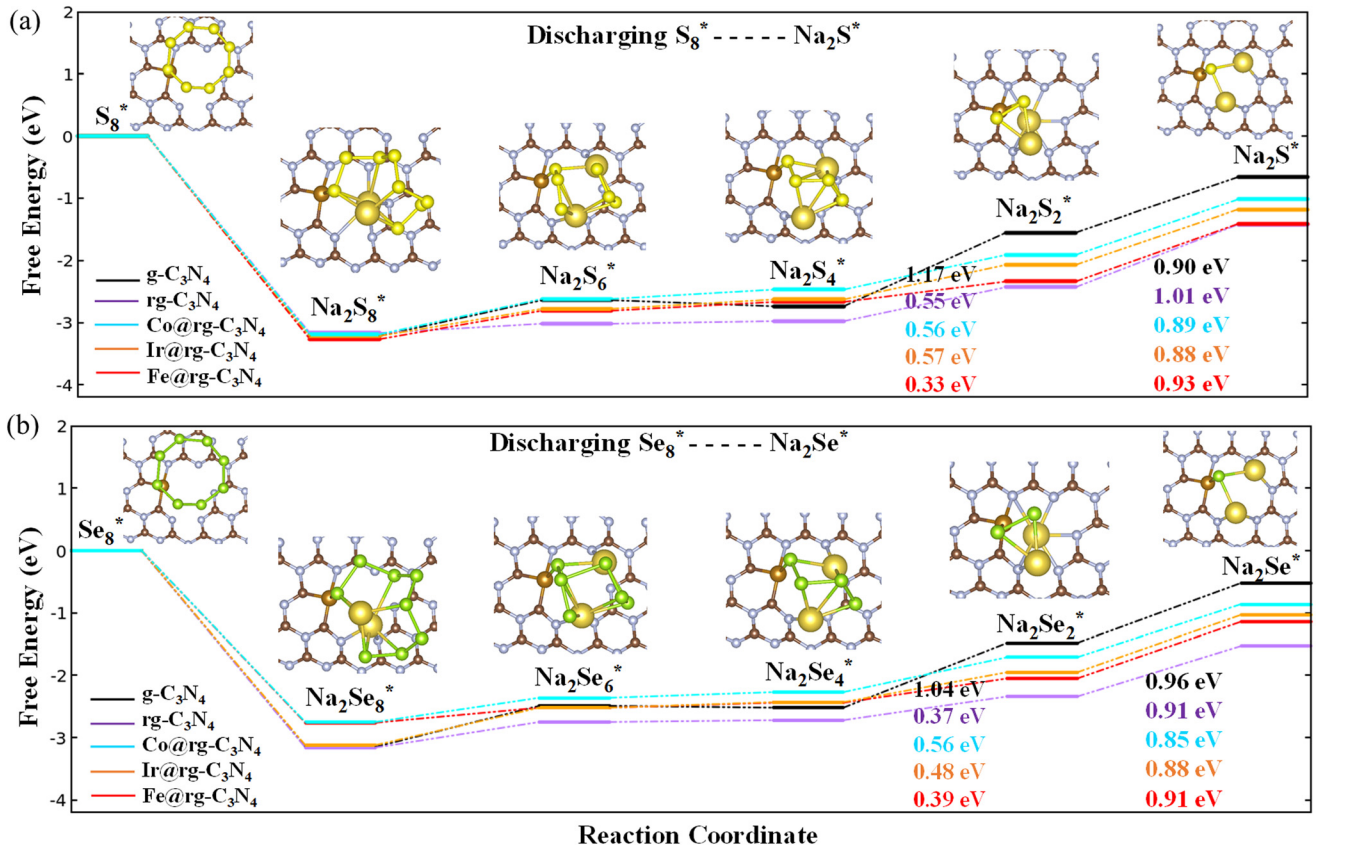

Fig. 4 Energy profiles for the reduction of (a) Na–pSs and (b) Na–pSes on g-C_3N_4, rg-C_3N_4 and SA@rg-C_3N_4 (SA = Co, Fe, Ir) monolayer. The inset images are the top view of Na–pXs adsorbed on the substrates.

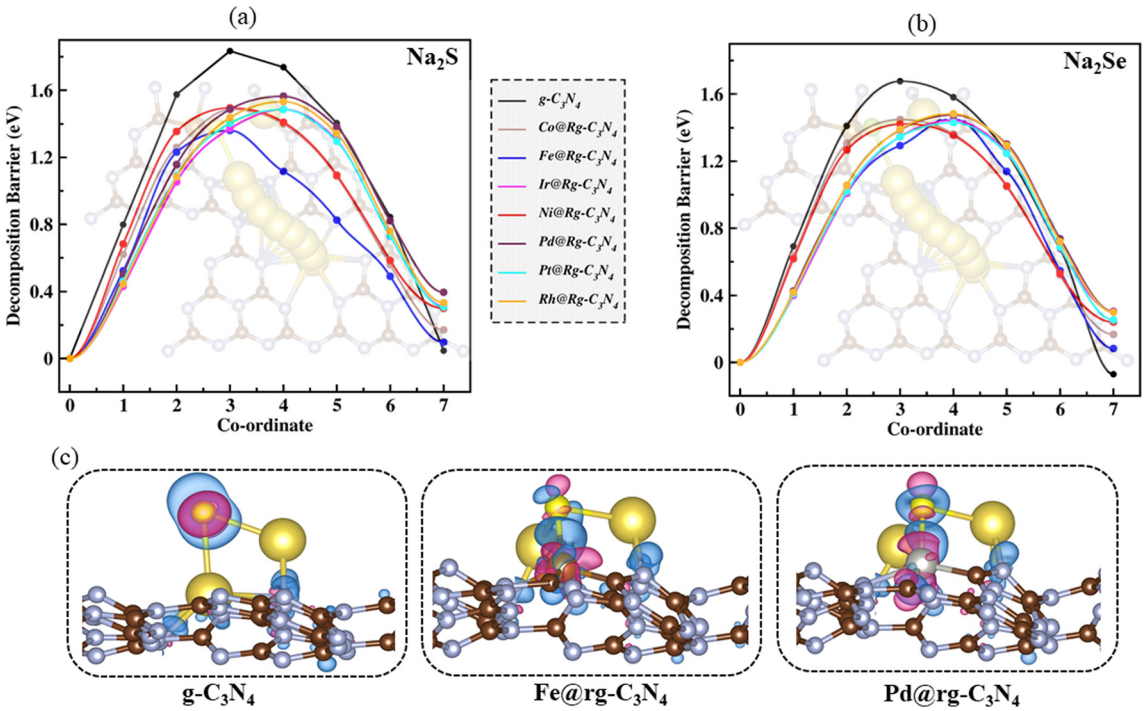

Fig. 5 Decomposition paths and decomposition energies of (a) Na_2S and (b) Na_2Se on the pristine g-C_3N_4 and SA@rg-C_3N_4 monolayers. (c) The charge density differences of Na_2S adsorbed on the pristine g-C_3N_4 and SA@rg-C_3N_4 monolayer. The blue regions represent electron accumulation, and magenta regions represent depletion.

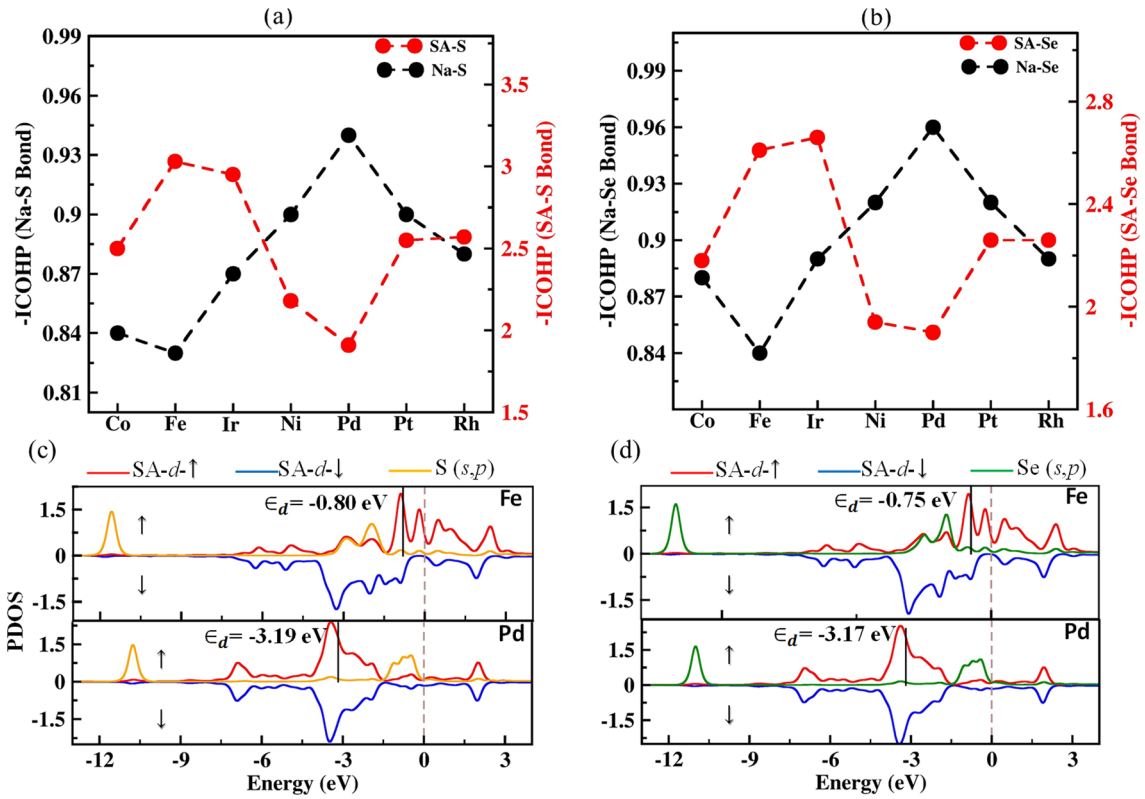

Fig. 6 The strength of (a) Na–S and SA–S bonds and (b) Na–Se and SA–Se evaluated using the integrated COHP (–ICOHP) for the Na_2X–SAC system. (Here, the depicted bond strength (–ICOHP) is the sum of the spin-up and spin-down –ICOHP values in eV per bond.) (c and d) The calculated partial density of states (PDOS) of Na_2X–SAC (SAC = Fe, Pd) systems. The up-spin d-band center values are illustrated on the PDOS plot, measured with respect to the Fermi level set at zero.

are significantly lower than in both g-C_3N_4 (1.83 eV for Na_2S and 1.68 eV for Na_2Se) and rg-C_3N_4 substrate (2.69 eV for Na_2S and 2.53 eV for Na_2Se). Furthermore, in Fig. 5(c) we show the charge density difference, defined as $\Delta\rho = \rho_{total} - \rho_{substrate} - \rho_{Na-pXs}$,[73] where ρ_{total}, $\rho_{substrate}$, and ρ_{Na-pXs} stand for the charge densities of the Na–pXs (X = S, Se) molecule adsorbed on the SA@rC_3N_4 substrate, the SA@rC_3N_4 substrate, and the isolated Na–pXs molecule, respectively. Fig. 5c, indicates that in the case of pristine g-C_3N_4, the charge transfer occurs predominantly between Na atoms and the substrate. However, for the SAC substrates, in addition to electron transfer from Na to the substrate, there is also a substantial flow of electrons between S and the metal atom (SA). It is worth noting that the electron transfer is more pronounced in Fe–S than in Pd–S bonds. This increased electron transfer between S and the SA atom can lead to the formation of a S–SA bond and a weakening the Na–S bond.

To further investigate the Na_2X decomposition mechanism on different SAC substrates, the intensity of Na–X and SA–X on various SACs substrates is evaluated using the Integrated of Crystal Orbital Hamilton Population (ICOHP) analysis.[74,75] For clarity, on Fig. 6(a) and (b), we present the negative values of the ICOHP results, –ICOHP, in units of eV per bond. Therefore, larger values of –ICOHP represent stronger interatomic interactions. The results shown in Fig. 6(a) and (b) suggest that the strength of both the SA–S and SA–Se bonds is largest for Fe among all other SACs, in agreement with our previous analysis. Conversely, for Na–X bonds, –ICHOP results reveal the opposite trend, *i.e.*, this interaction is weakest for Fe. Additionally, the Na–X bond strength (–ICOHP = 0.95 eV for Na_2S and 0.96 eV for Na_2Se) is larger in pristine g-C_3N_4 than in SACs based substrates, in agreement with the decomposition barriers results. The bonding interactions are further explored by plotting the partial density of states (PDOS) for SACs to reveal the electronic states of the SA and X (S, Se) atom. The strength of the SA–X interaction can be correlated to the position of the antibonding state (relative to the Fermi level), where a closer position of the antibonding state to the Fermi level can indicate a stronger SA–X interaction. The d-band model is extensively utilized to elucidate bond formation and reactivity patterns observed in transition metals.[76] Results presented in Fig. 6(c) and (d) show that the d-band centers (ε_d) of Fe are closer to the Fermi level than in other SACs. This proximity results in a stronger interaction between X and Fe, in agreement with the calculated decomposition barriers and binding strengths and the consequent weakening of the Na–X bonds in Na_2X. The remaining PDOS for Na_2X–SAC (SAC = Co, Ir, Rh, Ni, and Pt) are presented in Fig. S13.†

4. Conclusions

In summary, first-principles calculations are performed to elucidate the charging and discharging kinetics of SACs embedded on reduced g-C_3N_4 for Na–S and Na–Se electrodes. Through an analysis of Na–pS/Ses adsorption energies, the anchoring functionality of rg-C_3N_4 monolayer is found to be enhanced through the incorporation of SACs. AIMD simulations are performed to better understand the adsorption behaviour of S_8 and Se_8 species at the early stages of discharge and indicate no significant occurrence of sulfur or selenium poisoning on the surface of Fe, Co, Ir, Ni, Pt, and Rh SACs.

During the discharge process, the Gibbs free energy of the rate-limiting step of S/Se reduction reactions on the SACs is greatly reduced compared to the pristine g-C_3N_4 and rg-C_3N_4 surfaces, indicating a higher catalytic activity in the SACs substrates.

For the charging of S and Se electrodes, our results indicate that SACs substrates present a lower decomposition energy barrier for Na_2S and Na_2Se indicating a faster charging process of Na–S and Na–Se electrodes. These results are further supported by our ICOHP, PDOS, and d-band center analysis of Na_2S and Na_2Se adsorbed on SAC substrates.

This study offers solutions to the performance limitations caused by the shuttle effect and proposes an effective approach for optimizing single-atom catalysts to enhance the efficiency of sodium–sulfur and sodium–selenium electrodes.

Conflicts of interest

There are no conflicts to declare.

Acknowledgements

The authors acknowledge the support of the Automotive Research Center (ARC), Cooperative Agreement W56HZV-19-2-0001 U.S. Army DEVCOM GVSC. DISTRIBUTION STATEMENT A. Approved for public release; distribution is unlimited. OPSEC#8405. We acknowledge the computational resources and services provided by the Institute for Cyber-Enabled Research at Michigan State University.

References

1 J. Bi, Z. Du, J. Sun, Y. Liu, K. Wang, H. Du, W. Ai and W. Huang, *Adv. Mater.*, 2023, **35**, 2210734.
2 Y.-K. Liu, C.-Z. Zhao, J. Du, X.-Q. Zhang, A.-B. Chen and Q. Zhang, *Small*, 2023, **19**, 2205315.
3 J. Neumann, M. Petranikova, M. Meeus, J. D. Gamarra, R. Younesi, M. Winter and S. Nowak, *Adv. Energy Mater.*, 2022, **12**, 2102917.
4 N. T. Aristote, X. Deng, K. Zou, X. Gao, R. Momen, F. Li, W. Deng, H. Hou, G. Zou and X. Ji, *J. Alloys Compd.*, 2022, **913**, 165216.
5 R. Wang, D. Wang, Y. Dong, B. Xie, X. Wu, Q. Wu, S. Zhu, G. Diao and M. Chen, *J. Alloys Compd.*, 2023, **952**, 169980.
6 L. Jingjing, L. Hongji, H. Qiang and C. Zhe, *Prog. Chem.*, 2022, **34**, 857.
7 P. Chen, C. Wang and T. Wang, *Mater. Res. Lett.*, 2022, **10**, 691–719.

8 P. Hu, F. Xiao, Y. Wu, X. Yang, N. Li, H. Wang and J. Jia, *Chem. Eng. J.*, 2022, **443**, 136257.
9 G. Wang, Y. Chen, S. Yuan and P. Ge, *Molecules*, 2022, **27**, 5880.
10 Z. Huang, P. Jaumaux, B. Sun, X. Guo, D. Zhou, D. Shanmukaraj, M. Armand, T. Rojo and G. Wang, *Electrochem. Energy Rev.*, 2023, **6**, 21.
11 J. Xu, Y. Qiu, J. Yang, H. Li, P. Han, Y. Jin, H. Liu, B. Sun and G. Wang, *Adv. Funct. Mater.*, 2024, **34**, 2306206.
12 Z. Wu, X. Lin, J. Zhang, X. Chu, J. Xu, J. Li, Y. Liu, H. Yu, L. Yan, L. Zhang, *et al.*, *Chem. Eng. J.*, 2023, **454**, 140433.
13 C. Wu, Y. Lei, L. Simonelli, D. Tonti, A. Black, X. Lu, W.-H. Lai, X. Cai, Y.-X. Wang, Q. Gu, *et al.*, *Adv. Mater.*, 2022, **34**, 2108363.
14 Z. Yan, L. Zhao, Y. Wang, Z. Zhu and S.-L. Chou, *Adv. Funct. Mater.*, 2022, **32**, 2205622.
15 Y. Wang, D. Zhou, V. Palomares, D. Shanmukaraj, B. Sun, X. Tang, C. Wang, M. Armand, T. Rojo and G. Wang, *Energy Environ. Sci.*, 2020, **13**, 3848–3879.
16 R. Fang, J. Xu and D.-W. Wang, *Energy Environ. Sci.*, 2020, **13**, 432–471.
17 L. Wang, X. Zhang, L. Deng, J. Tang, H. Deng, W. Hu and Z. Liu, *ACS Appl. Mater. Interfaces*, 2019, **11**, 4995–5002.
18 J. Ding, H. Zhou, H. Zhang, T. Stephenson, Z. Li, D. Karpuzov and D. Mitlin, *Energy Environ. Sci.*, 2017, **10**, 153–165.
19 Q. Xu, H. Liu, W. Du, R. Zhan, L. Hu, S. Bao, C. Dai, F. Liu and M. Xu, *Electrochim. Acta*, 2018, **276**, 21–27.
20 X. L. Huang, Y.-X. Wang, S.-L. Chou, S. X. Dou and Z. M. Wang, *Energy Environ. Sci.*, 2021, **14**, 3757–3795.
21 M. S. Nahian, R. Jayan and M. M. Islam, *ACS Catal.*, 2022, **12**, 7664–7676.
22 F. Jin, B. Wang, J. Wang, Y. Wang, Y. Ning, J. Yang, Z. Zhang, P. Liu, Y. Zhou, D. Wang, *et al.*, *Matter*, 2021, **4**, 1768–1800.
23 C. Wang, T. Li, X. Hou, M. Jiang, Q. Zheng and X. Li, *Chem. Eng. J.*, 2023, **451**, 139062.
24 H. Tian, A. Song, H. Tian, J. Liu, G. Shao, H. Liu and G. Wang, *Chem. Sci.*, 2021, **12**, 7656–7676.
25 Z. Du, X. Chen, W. Hu, C. Chuang, S. Xie, A. Hu, W. Yan, X. Kong, X. Wu, H. Ji, *et al.*, *J. Am. Chem. Soc.*, 2019, **141**, 3977–3985.
26 Y. Li, J. Wu, B. Zhang, W. Wang, G. Zhang, Z. W. Seh, N. Zhang, J. Sun, L. Huang, J. Jiang, *et al.*, *Energy Storage Mater.*, 2020, **30**, 250–259.
27 Z. Zeng, W. Nong, Y. Li and C. Wang, *Adv. Sci.*, 2021, **8**, 2102809.
28 T. Duan, L. Wang, Z. Ma and Y. Pei, *Small*, 2023, **19**, 2303760.
29 I. Choudhuri, P. Bhauriyal and B. Pathak, *Chem. Mater.*, 2019, **31**, 8260–8285.
30 Z. Chen, J. Zhao, C. R. Cabrera and Z. Chen, *Small Methods*, 2019, **3**, 1800368.
31 D. Zeng, W. Xu, W.-J. Ong, J. Xu, H. Ren, Y. Chen, H. Zheng and D.-L. Peng, *Appl. Catal., B*, 2018, **221**, 47–55.
32 W. Sun, Z. Song, Z. Feng, Y. Huang, Z. J. Xu, Y.-C. Lu and Q. Zou, *Nano–Micro Lett.*, 2022, **14**, 222.
33 M. Jyothirmai, D. Roshini, B. M. Abraham and J. K. Singh, *ACS Appl. Energy Mater.*, 2023, **6**, 5598–5606.
34 H. Niu, X. Wan, X. Wang, C. Shao, J. Robertson, Z. Zhang and Y. Guo, *ACS Sustainable Chem. Eng.*, 2021, **9**, 3590–3599.
35 Y. Lu, H. Wang, P. Yu, Y. Yuan, R. Shahbazian-Yassar, Y. Sheng, S. Wu, W. Tu, G. Liu, M. Kraft, *et al.*, *Nano Energy*, 2020, **77**, 105158.
36 S. He, J. Yang, S. Liu, X. Wang, X. Che, M. Wang and J. Qiu, *Chem. Eng. J.*, 2023, **454**, 140202.
37 W.-W. Liu, S.-T. Niu, Z.-Q. Xu, R. Zou, C.-Y. Cui, Y.-X. Lei, X.-B. Zhang and F. Ran, *Appl. Surf. Sci.*, 2023, **609**, 155327.
38 P. Zhou, F. Lv, N. Li, Y. Zhang, Z. Mu, Y. Tang, J. Lai, Y. Chao, M. Luo, F. Lin, *et al.*, *Nano Energy*, 2019, **56**, 127–137.
39 X. Chen, X. Zhao, Z. Kong, W.-J. Ong and N. Li, *J. Mater. Chem. A*, 2018, **6**, 21941–21948.
40 G. Kresse and J. Furthmüller, *Phys. Rev. B: Condens. Matter Mater. Phys.*, 1996, **54**, 11169.
41 G. Kresse and J. Furthmüller, *Comput. Mater. Sci.*, 1996, **6**, 15–50.
42 J. P. Perdew, K. Burke and M. Ernzerhof, *Phys. Rev. Lett.*, 1996, **77**, 3865.
43 P. E. Blöchl, *Phys. Rev. B: Condens. Matter Mater. Phys.*, 1994, **50**, 17953.
44 S. Grimme, J. Antony, S. Ehrlich and H. Krieg, *J. Chem. Phys.*, 2010, **132**, 154104.
45 N. Yamsang, J. Sittiwong, P. Srifa, B. Boekfa, M. Sawangphruk, T. Maihom and J. Limtrakul, *Appl. Surf. Sci.*, 2021, **565**, 150378.
46 Y. Cheng, Y. Dou, D. Kan, Y. Wang and Y. Wei, *Appl. Surf. Sci.*, 2023, **610**, 155481.
47 G. D. Fao and J.-C. Jiang, *Mol. Catal.*, 2022, **526**, 112402.
48 G. Henkelman, B. P. Uberuaga and H. Jónsson, *J. Chem. Phys.*, 2000, **113**, 9901–9904.
49 G. Henkelman and H. Jónsson, *J. Chem. Phys.*, 2000, **113**, 9978–9985.
50 W. Tang, E. Sanville and G. Henkelman, *J. Phys.: Condens. Matter*, 2009, **21**, 084204.
51 A. Togo, F. Oba and I. Tanaka, *Phys. Rev. B: Condens. Matter Mater. Phys.*, 2008, **78**, 134106.
52 A. Togo and I. Tanaka, *Scr. Mater.*, 2015, **108**, 1–5.
53 S. Maintz, V. L. Deringer, A. L. Tchougréeff and R. Dronskowski, *J. Comput. Chem.*, 2016, **37**, 1030–1035.
54 V. Wang, N. Xu, J.-C. Liu, G. Tang and W.-T. Geng, *Comput. Phys. Commun.*, 2021, **267**, 108033.
55 K. Momma and F. Izumi, *J. Appl. Crystallogr.*, 2011, **44**, 1272–1276.
56 Y. Zhao and J. Zhao, *Appl. Surf. Sci.*, 2017, **412**, 591–598.
57 L. Song, M. Zhang and J. Guo, *Chem. Phys. Lett.*, 2021, **777**, 138711.
58 M. Jakhar, Y. Ding, B. D. Fahlman and V. Barone, *Nano Express*, 2024, **5**, 015028.
59 S. S. Batsanov, *Inorg. Mater.*, 2001, **37**, 871–885.

60 X. Song, D. Tian, Y. Qiu, X. Sun, B. Jiang, C. Zhao, Y. Zhang, L. Fan and N. Zhang, *Energy Storage Mater.*, 2021, **41**, 248–254.
61 C. Wei, M. Ge, T. Fang, X. Tang and X. Liu, *Phys. Chem. Chem. Phys.*, 2023, **25**, 24948–24959.
62 N. Li, Y. Zhan, H. Wu, J. Fan and J. Jia, *Nanoscale*, 2022, **14**, 17027–17035.
63 M. Sajjad, T. Hussain, N. Singh and J. A. Larsson, *Langmuir*, 2020, **36**, 13104–13111.
64 R. Jayan and M. M. Islam, *J. Phys. Chem. C*, 2021, **125**, 4458–4467.
65 N. Li, Y. Zhan, H. Wu, J. Fan and J. Jia, *Nanoscale*, 2023, **15**, 2747–2755.
66 R. Jayan and M. M. Islam, *ACS Appl. Mater. Interfaces*, 2021, **13**, 35848–35855.
67 T. Kaewmaraya, T. Hussain, R. Umer, Z. Hu and X. Zhao, *Phys. Chem. Chem. Phys.*, 2020, **22**, 27300–27307.
68 S. Mukherjee, L. Kavalsky, K. Chattopadhyay and C. V. Singh, *Nanoscale*, 2018, **10**, 21335–21352.
69 Y. Liu, Y. Elias, J. Meng, D. Aurbach, R. Zou, D. Xia and Q. Pang, *Joule*, 2021, **5**, 2323–2364.
70 H. Liu, W.-H. Lai, Q. Yang, Y. Lei, C. Wu, N. Wang, Y.-X. Wang, S.-L. Chou, H. K. Liu and S. X. Dou, *Nano–Micro Lett.*, 2021, **13**, 121.
71 G. Zhou, S. Zhao, T. Wang, S.-Z. Yang, B. Johannessen, H. Chen, C. Liu, Y. Ye, Y. Wu, Y. Peng, *et al.*, *Nano Lett.*, 2019, **20**, 1252–1261.
72 M. S. Nahian, R. Jayan, T. Kaewmaraya, T. Hussain and M. M. Islam, *ACS Appl. Mater. Interfaces*, 2022, **14**, 10298–10307.
73 Z. Yi, F. Su, L. Huo, G. Cui, C. Zhang, P. Han, N. Dong and C. Chen, *Appl. Surf. Sci.*, 2020, **503**, 144446.
74 V. L. Deringer, A. L. Tchougréeff and R. Dronskowski, *J. Phys. Chem. A*, 2011, **115**, 5461–5466.
75 M. Tachibana, K. Yoshizawa, A. Ogawa, H. Fujimoto and R. Hoffmann, *J. Phys. Chem. B*, 2002, **106**, 12727–12736.
76 S. Bhattacharjee, U. V. Waghmare and S.-C. Lee, *Sci. Rep.*, 2016, **6**, 35916.